

Theoretical Design of a Multifunctional Two-Dimensional HfGeTe₄-Based Optoelectronic Device Utilizing the Anisotropic Photogalvanic Effect

Degao Xu,¹ Jindou Ru,² Biao Cai,¹ Jianing Tan,¹ Kaike Yang,¹ Guowei Yang³, and Gang Ouyang^{1,*}

¹Key Laboratory of Low-Dimensional Quantum Structures and Quantum Control of Ministry of Education, Key Laboratory for Matter Microstructure and Function of Hunan Province, School of Physics and Electronics, Hunan Normal University, Changsha 410081, China

²Hongzhiwei Technology (Shanghai) Co. Ltd., 1599 Xinjinqiao Road, Pudong, Shanghai 201206, China

³State Key Laboratory of Optoelectronic Materials and Technologies, School of Materials Science and Engineering, Sun Yat-sen (Zhongshan) University, Guangzhou 510275, China



(Received 16 June 2023; revised 23 October 2023; accepted 30 October 2023; published 13 November 2023)

Achieving desirable multifunctional optoelectronic devices requires consideration of indexes such as photoelectrical response, polarization sensitivity, energy consumption, power conversion efficiency (PCE), and direction dependence. To satisfy these requirements, we propose an anisotropic HfGeTe₄-based optoelectronic device driven by the anisotropic photogalvanic effect (PGE) for high-performance photodetection and solar harvesting. We find a robust anisotropic PGE photocurrent J_{ph} ($J_x = 5.12$, and $J_y = 0.07$) is generated under the illumination of linearly polarized light due to the noncentrosymmetric nature of pristine HfGeTe₄. Through appropriate mechanical bending and heterostructure assembled with a black phosphorus monolayer, the photocurrent and anisotropic ratio can be substantially enhanced by 8 times and 22.98%, respectively. Moreover, it exhibits a very high PCE of 20.19% and a large optical conductivity of about $13 \times 10^3 \Omega^{-1} \text{ cm}^{-1}$. Our results show a fascinating functional coupling architecture that simultaneously implements high polarization-resolved photodetection and solar-energy harvesting in self-powered low-dimensional devices, suggesting an efficient avenue to achieve multifunctional integrated optoelectronic devices.

DOI: 10.1103/PhysRevApplied.20.054025

I. INTRODUCTION

Electronic devices have gradually developed in the direction of miniaturization, integrated, and multifunctional in the post-Moore era. On account of the numerous advantages of tunable electronic band structures, high surface-to-volume ratios, outstanding carrier-transport capability, excellent flexibility, high transparency, etc., two-dimensional (2D) van der Waals materials have stimulated a surge in research interest in the field of solar harvesting and polarization-resolved photodetection based on conversion mechanisms of “light to current” [1–5]. In view of 2D materials’ superior performance and fascinating physics, emerging 2D optoelectronic devices have established themselves as transformative building blocks toward photodetection [6–8], solar cells [9,10], and spin optoelectronics [11,12].

The typical conversion mechanisms of “light to current” are realized by the effect of photovoltaic, photoconductor, photogate, and photothermal in photonic devices [13–17], in which the traditional *p-n* junctions or external voltage is

required to generate the persistent photocurrent. The power conversion efficiency (PCE) of *p-n* junctions has been improved considerably in recent years and almost close to the Shockley-Queisser limitation [18]. 2D optoelectronic devices with an external voltage usually generate a dark current that may even exceed the photocurrent itself, which then largely degrades the signal-to-noise ratio [19]. In contrast to these typical “light-to-current” conversion mechanisms, the photogalvanic effect (PGE) [20–23], also called the bulk photovoltaic effect [24–27], which occurs in materials lacking spatial inversion symmetry, enables the generation of persistent photocurrent without external voltage or self-built internal field that is induced by *p-n* junctions. Because of the absence of spatial inversion symmetry, the sub-band electrons governed by the optical selection rules accept the unequal distribution of angular momentum of photon in the conduction band, which can lead to a net photocurrent.

The PGE is an alternative optical response derived from the nonlinear and symmetrical induction of materials to light. As a result, the imbalanced distribution of photoexcited electrons provides an open-circuit voltage larger than the band gap [28,29], which makes it possible for

*gangouy@hunnu.edu.cn

“light-to-current” conversion efficiency to overcome the Shockley-Queisser limitation [30]. The PGE with these advantages has triggered a great deal of research interest in 2D systems as a result of its promising applications in a variety of fields, including solar cells [31,32], photodetection [33,34], as well as spintronics [35–39]. Recent experimental and theoretical reports have demonstrated that the magnitude of PGE photocurrent can be substantially enhanced by strain [32,40–42], vacancy [43–45], doping [46,47], and construction of heterostructures [48–51], which mainly are ascribed to the reduction of crystal symmetry. Nevertheless, the tiny photocurrent prevailing in the pristine structure still limits its practical application.

Recently, 2D ternary chalcogenides have been considerably explored due to their distinctive structures and exotic properties, which are attributed to the stoichiometric variation and increased elemental degrees of freedom. The layered ternary transition-metal chalcogenide, HfGeTe₄, has been successfully synthesized, and its crystal structure has been determined via single-crystal x-ray diffraction techniques [52]. The monolayer of HfGeTe₄ (ML-HfGeTe₄) has garnered significant attention in research owing to its suitable direct band gap, ultrasoft property, remarkable carrier mobility, and optical absorption capacity [53–55]. More significantly, the quasi-one-dimensional chainlike structure of ML-HfGeTe₄ are believed to foster strong in-plane anisotropy and ultralow symmetry [56,57]. The strong anisotropy is essential to achieve a high-polarization sensitivity photodetector. Meanwhile, the ultralow symmetry is very conducive to the substantial enhancement of PGE. However, the investigation of the physical origin of anisotropic optoelectronic properties in ML-HfGeTe₄ is still in its infancy. Also, it currently remains elusive that the pristine structure is purposely designed to lose spatial inversion symmetry under the synergistic effect of anisotropy and asymmetry, which can achieve a fascinating multifunctional coupling architecture.

In this study, we propose a multifunctional optoelectronic device based on ML-HfGeTe₄ that can simultaneously improve the photoelectric response, solar harvesting, anisotropy, polarization sensitivity, and photoconductivity due to the synergistic effect of anisotropy and asymmetry. Our quantum transport simulations indicate that the pristine HfGeTe₄ photodetector can produce a PGE photocurrent of 5.12 and an anisotropic ratio of 73, which can be further enhanced by 8 times and 22.98%, through mechanical bending and assemble heterostructure with a monolayer of black phosphorus (ML-BP). Furthermore, it exhibits type-II band alignment and PCE of 20.19%, implying that the multifunctional applications of self-power photodetections and solar harvesting can be achieved using BP/HfGeTe₄ heterostructure.

II. MODEL AND METHODS

The pristine ML-HfGeTe₄ is orthorhombic with the lattice constants a of 11.09 Å and b of 4.01 Å. The ML-HfGeTe₄ belongs to the noncentrosymmetric C_s group. The sketch of the ML-HfGeTe₄ photodetector is shown in Fig. 1, which can be divided into three parts, i.e., the left- and right-handed leads as well as the central region. Note that the two-probe systems along the transport direction extend to $z = \pm\infty$. To account for the anisotropic PGE of ML-HfGeTe₄, we define the lattice constant a to be the x direction, and the y direction as consistent with the shorter lattice b vector. The supercells of $3 \times 1 \times 1$ and $1 \times 8 \times 1$ are adopted in the scattering regions along the x and y directions, respectively. Figures 1(a)–1(d) are the top and front views of the device along the x and y directions, respectively. It has been shown that the exceptional flexibility of ML-HfGeTe₄ both in plane and out of plane in our previous results ($C_{11}=42.02$ N m⁻¹, $C_{22}=65.00$ N m⁻¹, $C_{66}=14.14$ N m⁻¹) [57], renders it highly appropriate for deployment in flexible nanodevices. To intentionally decrease the spatial inversion symmetry of ML-HfGeTe₄ and amplify the PGE, mechanical bending is utilized to impose a central angle of 30° on the ML-HfGeTe₄ devices (ML-HfGeTe₄ bending) along the x and y directions, respectively. The ML-HfGeTe₄ bending in the y direction is fully relaxed as shown in Fig. 4(a). Furthermore, constructing heterostructures using ML-BP

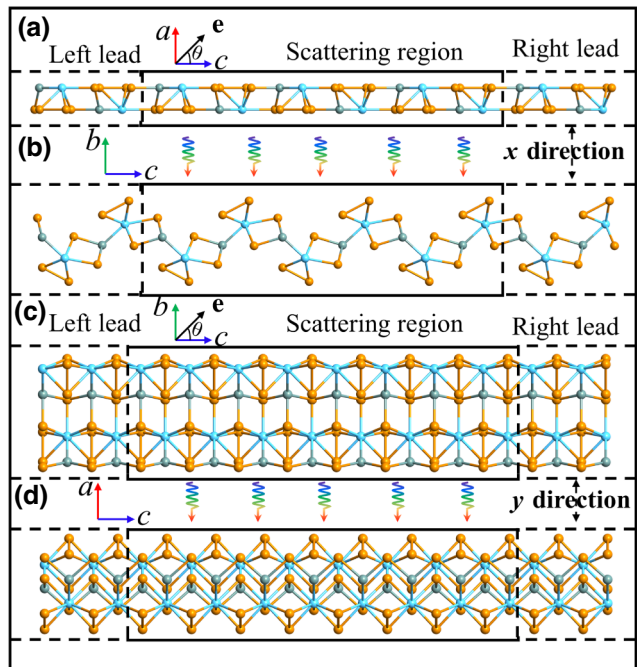


FIG. 1. Top and side views of ML-HfGeTe₄ device in the (a),(b) x and (c),(d) y directions, respectively.

is also investigated as a means to reduce device symmetry. The lattice parameters of ML-BP unit cells are $a = 4.62 \text{ \AA}$ and $b = 3.30 \text{ \AA}$, which are consistent with previous work [48]. For the case of BP/HfGeTe₄ heterostructure, the supercells of $\sqrt{8} \times \sqrt{5}$ and 1×2 are used for ML-BP and ML-HfGeTe₄, respectively. Therefore, the lattice parameters of the BP/HfGeTe₄ superlattice are obtained to be $a = 11.16 \text{ \AA}$, $b = 8.02 \text{ \AA}$, with the overall lattice mismatch of 1.06%, and the vertical distance between layers is 3.13 Å. The sketch of the BP/HfGeTe₄ photodetector oriented along the x and y directions is depicted in Fig. S1 (see Supplemental Material for more details [58]). It is worth noting that the implementation of mechanical bending and construction of heterostructures can lead to the elimination of the mirror reflection plane of pristine ML-HfGeTe₄.

In our cases, we employed a plane-wave basis projector augmented wave method [61] within the Vienna *ab initio* simulation package (VASP) [62] to assess both structural relaxation and band dispersions. Perdew-Burke-Ernzerhof (PBE) is implemented to describe the exchange-correlation potential within the generalized gradient approximation (GGA) [63]. The kinetic energy cutoff for the plane wave was set to $\hbar^2|K + G|^2/2m = 500 \text{ eV}$. Brillouin-zone integration of ML-HfGeTe₄ and BP/HfGeTe₄ is executed with the $6 \times 16 \times 1$ and $8 \times 6 \times 1$ k -point grids determined by the Γ -centered Monkhorst-Pack scheme [64]. The geometric optimization and ionic relaxation until the Hellmann-Feynman forces on each atom were smaller than 0.01 eV Å⁻¹, and the energy difference between two sequential steps was less than 10^{-5} eV . The Heyd-Scuseria-Ernzerhof (HSE06) hybrid function is utilized to achieve accurate estimations of band gaps and band alignments. A vacuum thickness of approximately 25 Å was adopted along the out-of-plane direction to minimize the periodic interaction between the adjacent monolayers. The phonon dispersive relations by the small displacement method implemented in the PHONOPY package and the results are processed by the vaspkit package [65,66]. The *ab initio* molecular dynamics (AIMD) simulations with a total simulation time of 6 ps and time steps of 3 fs are used to examine the thermal stability of BP/HfGeTe₄.

The photoelectric properties generated by the PGE are investigated based on density-functional theory within the nonequilibrium Green's function method (NEGF) [67]. The electron-photon interaction can be considered in the Hamiltonian as $\hat{H} = \hat{H}_0 + (e/m_0)\mathbf{A} \cdot \hat{\mathbf{P}}$, where H_0 is the Hamiltonian without the electron-light interaction, e is the electron charge, m_0 is the free electron mass, and $\hat{\mathbf{P}}$ and \mathbf{A} are the momentum of the photoexcited electrons and the electromagnetic vector potential of polarized light, respectively. According to linear response theory [68], the photocurrent injected into the leads (label with L) can be

written as [69]

$$J_L^{(\text{ph})} = \frac{ie}{\hbar} \int Tr\{\Gamma_L[G^{<(\text{ph})} + f_L(G^{>(\text{ph})} - G^{<(\text{ph})})]\}dE. \quad (1)$$

In particular, when the central scattering region is irradiated by linearly polarized light, the photocurrent injected into the leads can be written as [36,48]

$$\begin{aligned} J_L^{(\text{ph})} = & \frac{ie}{\hbar} \int \{\cos^2\theta Tr\{\Gamma_L[G_1^{<(\text{ph})} + f_L(G_1^{>(\text{ph})} - G_1^{<(\text{ph})})]\} \\ & + \sin^2\theta Tr\{\Gamma_L[G_2^{<(\text{ph})} + f_L(G_2^{>(\text{ph})} - G_2^{<(\text{ph})})]\} \\ & + \frac{\sin(2\theta)}{2} Tr\{\Gamma_L[G_3^{<(\text{ph})} + f_L(G_3^{>(\text{ph})} - G_3^{<(\text{ph})})]\}\}dE, \end{aligned} \quad (2)$$

where

$$\begin{aligned} G_1^{>/<(\text{ph})} = & \sum_{\alpha,\beta=x,y,z} C_0 N G_0^r e_{1\alpha} p_\alpha^\dagger G_0^{>/<} e_{1\beta} p_\beta G_0^a, \\ G_2^{>/<(\text{ph})} = & \sum_{\alpha,\beta=x,y,z} C_0 N G_0^r e_{2\alpha} p_\alpha^\dagger G_0^{>/<} e_{2\beta} p_\beta G_0^a, \\ G_3^{>/<(\text{ph})} = & \sum_{\alpha,\beta=x,y,z} C_0 N (G_0^r e_{1\alpha} p_\alpha^\dagger G_0^{>/<} e_{2\beta} p_\beta G_0^a \\ & + G_0^r e_{2\alpha} p_\alpha^\dagger G_0^{>/<} e_{1\beta} p_\beta G_0^a). \end{aligned} \quad (3)$$

For circularly polarized light,

$$\begin{aligned} J_L^{(\text{ph})} = & \frac{ie}{\hbar} \int \{\cos^2\phi Tr\{\Gamma_L[G_1^{<(\text{ph})} + f_L(G_1^{>(\text{ph})} - G_1^{<(\text{ph})})]\} \\ & + \sin^2\phi Tr\{\Gamma_L[G_2^{<(\text{ph})} + f_L(G_2^{>(\text{ph})} - G_2^{<(\text{ph})})]\} \\ & + \frac{\sin(2\phi)}{2} Tr\{\Gamma_L[G_3^{<(\text{ph})} + f_L(G_3^{>(\text{ph})} - G_3^{<(\text{ph})})]\}\}dE, \end{aligned} \quad (4)$$

where $G_{1,2}^{>/<(\text{ph})}$ is the same as in the linearly polarized case and

$$\begin{aligned} G_3^{>/<(\text{ph})} = & \pm i \sum_{\alpha,\beta=x,y,z} C_0 N (G_0^r e_{1\alpha} p_\alpha^\dagger G_0^{>/<} e_{2\beta} p_\beta G_0^a \\ & - G_0^r e_{2\alpha} p_\alpha^\dagger G_0^{>/<} e_{1\beta} p_\beta G_0^a). \end{aligned} \quad (5)$$

Here, $C_0 = (e/m_0)^2 (\hbar\sqrt{\mu_r\xi}/2N\omega\xi c) I_\omega$, m_0 is the bare electron mass, ξ denotes the dielectric constant, N is the number of photons, $G_0^{r/a}(G_0^{>/<})$ are the retarded or advanced (greater or lesser) Green's functions without photons, $p_{x,y,z}$ is the Cartesian component of the electron momentum and $e_{1(2)x,y,z}$ is the Cartesian component of the polarization vector e . For the linearly polarized light,

$\mathbf{e} = \cos \theta \mathbf{e}_1 + \sin \theta \mathbf{e}_2$ with θ being the polarization angle. For elliptically polarized light, $\mathbf{e} = \cos \phi \mathbf{e}_1 \pm i \sin \phi \mathbf{e}_2$ with \pm is being the right- or left-handed elliptical light, and ϕ determines its helicity. Specifically, $\phi = \pm 45^\circ$ corresponds to circularly polarized light. For Figs. 1(a) and 1(b), the polarized light is irradiated vertically along the b axis in the scattering region of ML-HfGeTe₄ photodetector and the θ formed by the vector \mathbf{e} with respect to the a - c plane, the \mathbf{e}_1 and \mathbf{e}_2 are the unit vectors along the transport direction and periodic direction, respectively. The PGE photocurrent obtained can be further normalized by $J = J_L^{(\text{ph})}/eI_\omega$ with I_ω being the photon flux determined by the number of photons per unit area per unit time. Note that the normalized photocurrent still has dimensions of area, i.e., a_0^2/photon with a_0 being the Bohr radius. The normalized photocurrent can be converted to the actual photocurrent, as shown within the Supplemental Material [58]. To facilitate the comparison with the previous theoretical works, we then still use the normalized photocurrent.

The approach mentioned above to determine the PGE photocurrent can be carried out utilizing the quantum transport software package Nanodcal [67]. The double- ζ -polarized (DZP) basis set is selected to expand all pertinent physical properties, whereby a linear combination of atomic orbital basis is employed. To treat exchanges and correlations, we adopted a generalized gradient approximation with PBE form. The atomic cores are characterized by norm-conserving nonlocal pseudopotentials following the standard protocol. The electron temperature is set to 100 K, and the $1 \times 10 \times 100$ ($5 \times 1 \times 100$) k points are executed to sample the scattering region along the x (y) directions in the self-consistent field calculations. For the PGE photocurrent calculation, $1 \times 10 \times 1$ ($5 \times 1 \times 1$) k -point grids are correspondingly adopted.

III. RESULTS AND DISCUSSION

A. Anisotropic effect

The phonon dispersion of the fully relaxed ML-HfGeTe₄ is first calculated as presented in Fig. S2 within the Supplemental Material [58]. One can see that the ML-HfGeTe₄ photodetector here is dynamical stability due to the overall phonon dispersions are devoid of any imaginary frequencies. The ML-HfGeTe₄ in the GGA-PBE algorithm is a direct band-gap semiconductor with its value of 0.75 eV, and it can be refined further to 1.34 eV using HSE06 hybrid functional approach. The corresponding electronic band structures are given in Fig. S2(b) within the Supplemental Material [58]. Consequently, the sampled photon energy range is between 1.4 and 3.4 eV, which is larger than that of ML-HfGeTe₄ and covers the entire visible light spectrum.

Figures 2(a) and 2(b) show the PGE photocurrent of the ML-HfGeTe₄ photodetector in linearly polarized light along the x and y directions with 1.9, 2.6, and 3.4 eV as examples. We find that the photocurrent is sensitive under

illumination by linearly polarized light. The photocurrent maintains a perfect cosine (sine) dependence versus the polarization angle in the x (y) direction, which stems from a second-order response of C_s symmetry structures to the electric field of light, i.e.,

$$j_c = E_0^2 \chi_{cc(a/b)} \sin(2\theta), j_{(a/b)} = E_0^2 (\chi_+ + \chi_- \cos(2\theta)), \quad (6)$$

here, c is the transport direction of photogenerated carriers. j_c and $j_{(a)}$ or $j_{(b)}$ are the photocurrents along the directions normal and parallel to the mirror reflection plane, respectively. E_0^2 refers to the electric field amplitude of the light, and $\chi_{cc(a/b)}$, χ_+ , and χ_- denote the tensors that dependent on the photon frequency ω . Therefore, the characteristics of photocurrent either takes a sine or a cosine are determined by both symmetry and polarized light. Our results are in accordance with the phenomenological theory of PGE [20] that has been widely used to explain the behavior of PGE [70] in experiments. Specifically, when the photon energy of the linearly polarized light corresponds to the energy in our examples, we find that the ML-HfGeTe₄ photodetector has an anisotropic PGE photocurrent, which is one order of magnitude larger in the x direction than that in the y direction. Furthermore, the effect of circularly polarized light illumination on PGE photocurrent is also considered additionally, the results reveal that the helicity (ϕ) as a function of PGE photocurrent is almost identical to that of polarization angle (θ) at the same photoenergies, which agrees with the explanation given in the previous work [49], i.e., the characteristic of PGE here is determined by C_s symmetry. Note that for oblique incidence, the PGE responses of linearly and circularly polarized light at C_s symmetry will no longer be similar. Here, we consider only the PGE response of normal incidence to C_s symmetry. In this scenario, all subsequent calculations of the PGE response are discussed for linearly polarized light.

We then give, in Fig. 3(a), the maximum PGE photocurrents (J_{\max}) for different photon energies in the x and y directions. The occurrence of high anisotropic photoelectric properties is due to the evident difference in the x and y directions of photocurrent. The maximum photocurrent for x and y directions are 5.12 at 1.7 eV and 1.64 at 2.8 eV, respectively. This means that the valence-band electrons are favorable to be excited by 1.7 eV photons along the x direction, whereas, for the y direction, it is more likely to absorb 2.8-eV photons to be excited to the conduction band. The electron transmission coefficient (T_E) versus the energy is shown in Figs. 3(a) and 3(b). There are two T_E peaks at -1.05 and 0.65 eV along the x direction, also at -1.39 and 1.41 eV along the y direction, respectively. According to Fermi's golden rule, the T_E of electrons is proportional to the density of states (DOS), it means that the energy difference between the two peaks can generate large photocurrent due to the greater transmission probability. Thus, large PGE photocurrents in the

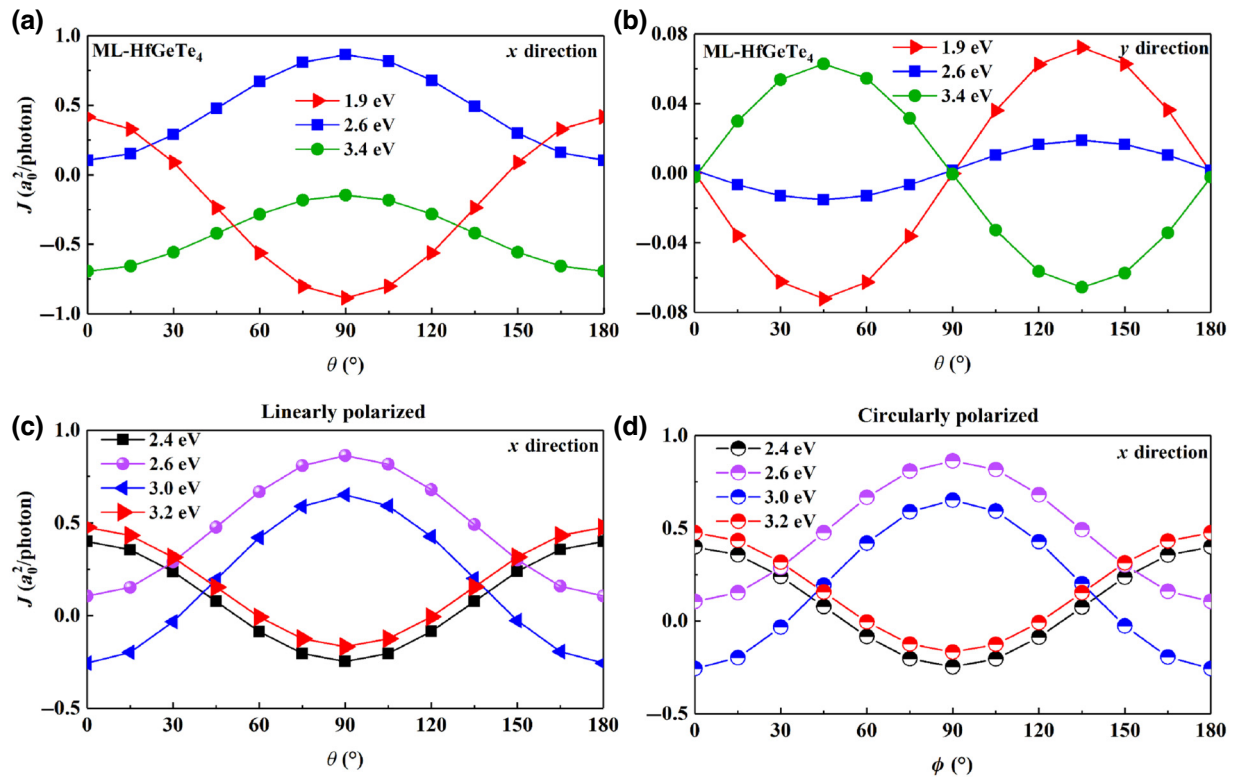


FIG. 2. The photocurrent of ML-HfGeTe₄ along the (a) x and (b) y directions for different photon energies under illumination by linearly polarized light. Comparison of (c) linearly and (d) circularly polarized light.

x and y directions occur at 1.7 and 2.8 eV, respectively. Note that the transmission spectrums of the ML-HfGeTe₄ photodetector along two different directions have a gap value close to the band gap of 0.75 eV near the Fermi level. It is clear that the devices constructed along different directions do not affect the electronic properties of pristine ML-HfGeTe₄, i.e., the direction-dependent PGE photocurrent is defined only by the anisotropic effects.

To ensure that the obtained results are reproducible and reasonable, the supercells of $6 \times 1 \times 1$ is adopted in the scattering regions of ML-HfGeTe₄ along the x directions. A schematic of the device and the PGE photocurrents response are shown in Fig. S3 within the Supplemental Material [58]. One can see that the photocurrent after cell expansion still follows the perfect cosine dependence in the x direction, and the maximum photocurrent is very close to the previous result. Note that the photocurrent and photon energy resonance peaks are shifted due to the expansion of unit cells in the central scattering region, which has no effect on the overall photoelectric performance of ML-HfGeTe₄. Furthermore, the effect of k -point sampling on the PGE photocurrent is also considered. The photocurrent of the ML-HfGeTe₄ device sampled at k -point grids of $1 \times 10 \times 1$ and $1 \times 20 \times 1$ in the x direction, and $5 \times 1 \times 1$ and $10 \times 1 \times 1$ in the y direction are calculated, as depicted in Fig. S4 within the Supplemental Material [58]. It is clear that the photocurrent is consistent

as the k -point grids increases, indicating that the k points have converged.

B. Mechanical bending effect

For structures lacking spatial inversion symmetry, the photoexcited electrons may experience an asymmetric motion in the conduction band that creates a nonequilibrium situation conducive to the generation of persistent photocurrent. In this sense, reducing the symmetry of the system by mechanical bending can potentially enhance the PGE photocurrent. For instance, it was experimentally confirmed that the PGE photocurrent of WS₂ nanotubes is several orders of magnitude higher than that of the pristine monolayer stems from the symmetry reduction from D_{2h} to C_{2nv} [32]. 2D optoelectronic devices are gradually developing towards a “flexible” future. Based on the pristine ML-HfGeTe₄ photodetector, noncollinear leads are constructed by bending the planar scattering region along x and y directions with a central angle of 30° (ML-HfGeTe₄ bending), as evident in Fig. 4(a). Figures 4(b) and 4(c) present example PGE photocurrent characteristics of the ML-HfGeTe₄-bending photodetector along the x and y directions for photoenergies of 1.7, 2.4, and 2.9 eV, respectively. As mentioned, the photocurrent J in the x direction varies as a function of $\alpha \cos(2\theta) + J_0$, and follows the $\beta \sin(2\theta) + J_0$ forms in the y direction. Although the PGE

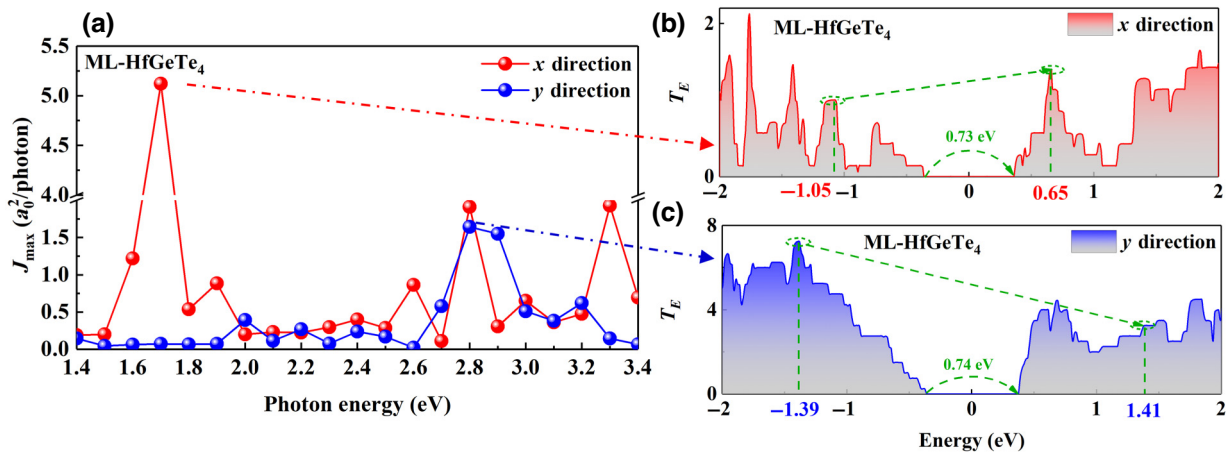


FIG. 3. (a) The maximum photocurrent of ML-HfGeTe₄ under different photon energies for the *x* and *y* directions. (b),(c) The electron transition spectrum of ML-HfGeTe₄ in the *x* and *y* directions, respectively.

photocurrent still maintains a $\cos(2\theta)$ dependence versus the polarization angle in the *x* direction, the photocurrent in the *y* direction is not proportional to $\sin(2\theta)$ at certain photon energy. Instead, j_z is proportional to $\sin(2\theta + \theta_0)$ with θ_0 being a phase shift that is caused by the buckling strain. Therefore, it can be seen that the maximum photocurrent in the *x* direction is 42.77 at $\theta = 90^\circ$ for 1.7 eV, and in the

y direction is 3.62 at $\theta = 90^\circ$ for 2.9 eV. Compared with the pristine ML-HfGeTe₄ device, the PGE photocurrent of the ML-HfGeTe₄-bending photodetector along the *x* and *y* directions is both enhanced dramatically.

The J_{\max} with respect to the different photon energies in the *x* and *y* directions are calculated, as depicted in Fig. 4(d). The J_{\max} is 42.77 at 1.7 eV for *x* direction and

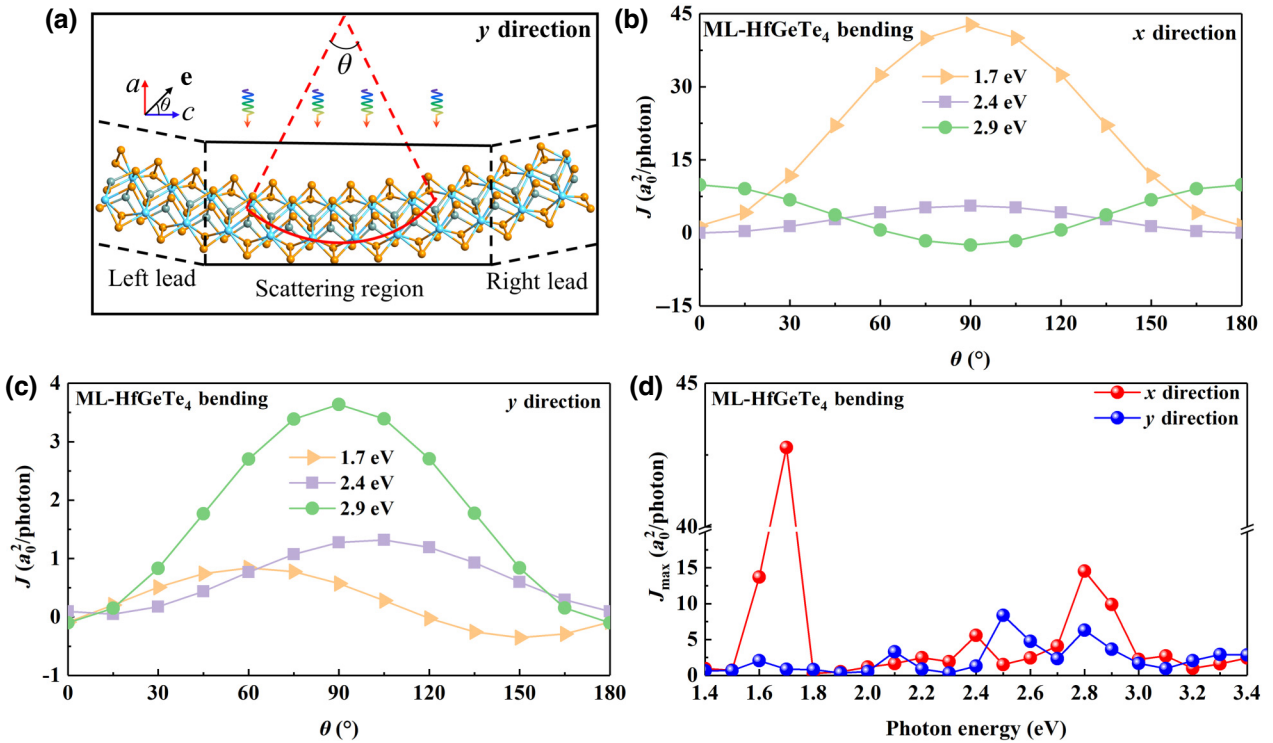


FIG. 4. (a) The side view of ML-HfGeTe₄ device under the condition of mechanical bending (central angle of 30°) along the *y* direction. (b) Dependence of photocurrent on polarization angle θ for ML-HfGeTe₄-bending along *x* and (c) *y* directions under different photon energies. (d) The maximum photocurrent of ML-HfGeTe₄ bending under different photon energies in the *x* and *y* directions.

8.37 at 2.5 eV for y direction. This means that the performance of the pristine ML-HfGeTe₄ photodetector in both x and y directions can be enhanced by about 8 times as its symmetry is reduced from C_s to C_1 by the buckling strain. Interestingly, the mechanical bending enhances the PGE photocurrent without weakening the photoelectric anisotropic ratio. To obtain a deeper understanding of these results, we plot the local density of states (LDOS) of ML-HfGeTe₄-bending device in the central scattering region along the x and y directions (Fig. 5), respectively. The Fermi energy level is set at 0 eV, an evident band gap of approximately 0.75 eV is observed along both the x and y directions (blue area). This suggests that applying a small buckling strain to pristine ML-HfGeTe₄ photodetector has a negligible effect on the whole electronic band structure of the device, and reduces only its spatial inversion symmetry. Moreover, compared with the y direction, the distribution of the atomic DOS projected on the conduction bands along the x direction in the transport space plane (z) is very asymmetric, thus, the x direction has a larger PGE photocurrent. In addition, to reveal whether the regulation of bending strain on PGE photocurrent is affected by angle, the PGE response of bending with a central angle of 10° is calculated as shown in Fig. S5 within the Supplemental Material [58]. The photocurrent is significantly reduced in both the x and y directions compared to the bending of 30°. However, there is still a small increase of photocurrent under bending of 10° compared to that of pristine ML-HfGeTe₄. It shows that bending can effectively reduce the symmetry of the device and increase the PGE photocurrent under polarized light, and there is a positive correlation between PGE and bending strain.

C. Construct heterostructures

The anisotropic effect is considered to be one of the important strategies for designing multifunctional devices, as it introduces additional degrees of freedom for tuning electrical and optical properties. Thus, we investigate the potential of constructing a heterostructure for ML-HfGeTe₄ to induce a reduction in symmetry and enhancement in the anisotropic ratio within the device. As the inaugural anisotropic 2D material, BP has been demonstrated to possess anisotropic electronic, mechanical, and thermal properties [71–73]. Moreover, BP has garnered extensive utilization in optoelectronic devices [74,75], primarily attributed to its exceptional carrier mobility, broadband photoresponse, and inherent linear dichroism. We find that the utilization of supercells with $\sqrt{8} \times \sqrt{5}$ and 1×2 for ML-BP and ML-HfGeTe₄ can effectively regulate the lattice mismatch to 1.06%. The band structure and phonon band dispersions of ML-BP are depicted in Fig. S6 within the Supplemental Material [58]. The ML-BP shows a direct band gap of 0.91 eV under the PBE algorithm, while that of 1.60 eV under the approach of the HSE06

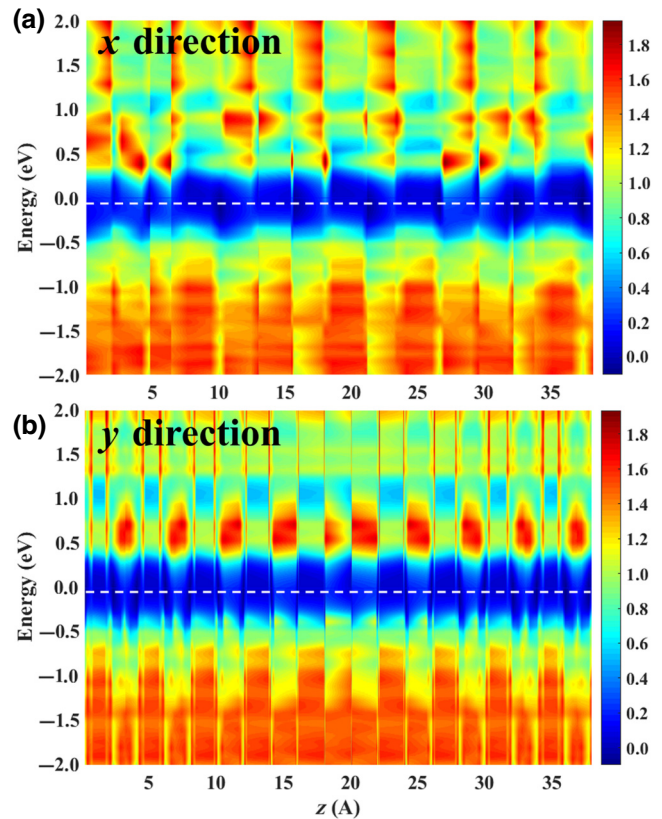


FIG. 5. (a),(b) The local density of states for the center region of ML-HfGeTe₄-bending device in the x and y directions, respectively. The Fermi level is set at 0 eV, indicated by the white dashed line.

framework, agreeing well with the previous results [76]. In addition, we calculate the direction-dependent photoelectric responses of pristine ML-BP photodetector, as shown in Fig. S7 within the Supplemental Material [58]. The results show that the J_{\max} in the armchair direction is 0.38, which is about one order of magnitude larger than that in the zigzag direction. Our conclusions are consistent with other work [49], with only certain differences at the corresponding peaks due to differences in the calculation parameters, we emphasize that our method is universal and reasonable, and that the choice of semiconductor is not restricted to BP or HfGeTe₄.

Next, the dependence of PGE photocurrent on polarization angle θ for direction-dependent BP/HfGeTe₄ photodetector at different photon energies (as examples, 1.5, 1.6, and 2.8 eV are given), as evident in Figs. 6(a) and 6(b). One can see that the photocurrent of 2.8 eV (red curve) is fitted well with the function $J = 3.26 + 5.87(\cos 2(\theta + 4^\circ))$ for x direction, and $J = 0.39 + 0.26(\sin 2(\theta - 30^\circ))$ for y direction. The shifting phase angle is arising from the symmetry decreasing from C_s to C_1 . The maximum photocurrent is therefore not located at 0° or 90° at certain photon energies. We then

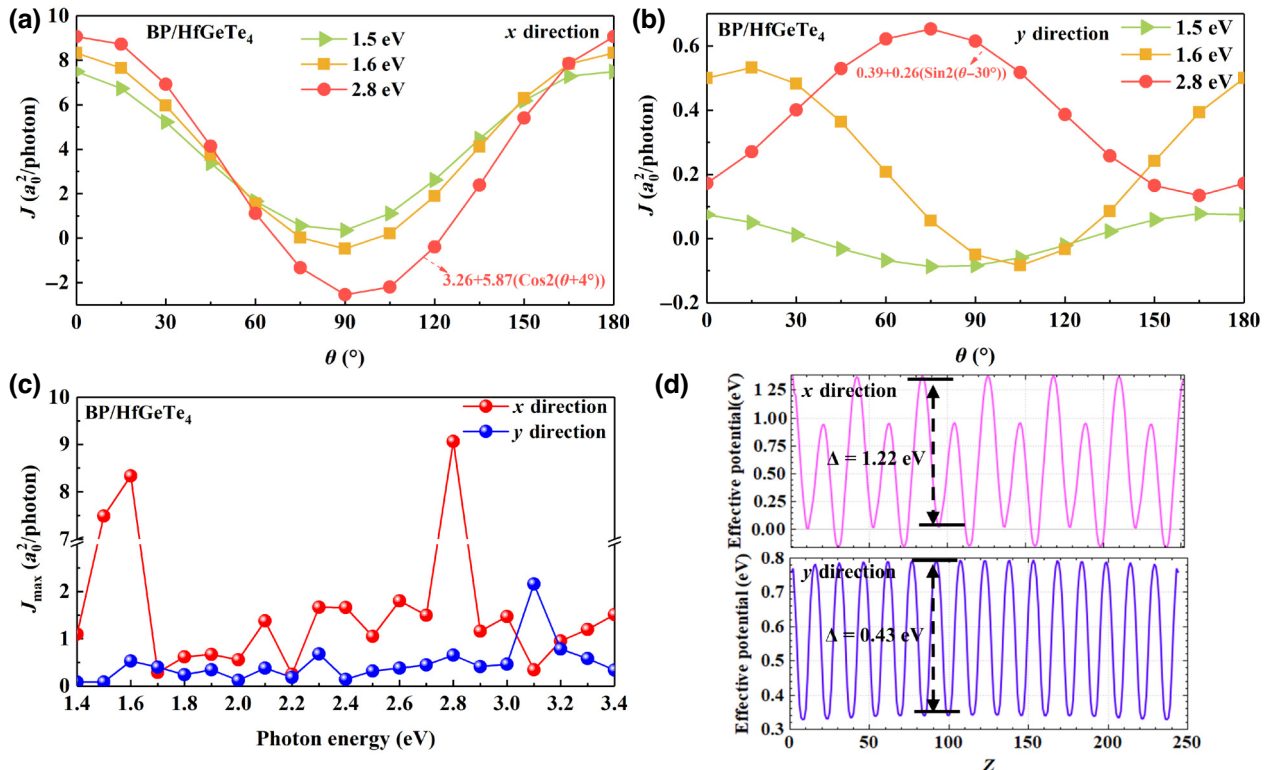


FIG. 6. (a) Dependence of photocurrent on polarization angle θ for BP/HfGeTe₄ device along the x and (b) y directions under different photon energies. (c) The maximum photocurrent of BP/HfGeTe₄ device under different photon energies in the x and y directions. (d) Hartree effective potential of BP/HfGeTe₄ in the x and y directions.

give, in Fig. 6(c), the J_{\max} for various photon energies in the x and y directions. There is evidently higher anisotropy than the pristine ML-HfGeTe₄ and ML-HfGeTe₄-bending cases between the x and y directions, with a maximum of 9.02 at 2.8 eV, and 2.10 at 3.1 eV, respectively. To shed light on the anisotropic photoelectric responses stemming from the device's symmetry, we present the Hartree effective potential along both x and y axes in Fig. 6(d). Clearly, it exhibits a considerably more symmetric and higher effective potential energy of 1.22 eV in the x direction as compared to that in the y direction, which shows a value of 0.43 eV. Consequently, this anisotropy can give rise to a larger photocurrent that is direction dependent.

To evaluate the overall performance of multifunctional polarized optoelectronic devices, we explore the polarization sensitivity and anisotropic ratio, which represent the critical device figure of merit. The extinction ratio (ER), defined as J_{\parallel}/J_{\perp} or J_{\perp}/J_{\parallel} , is proposed to measure the polarization sensitivity [Fig. 7(a)], where J_{\parallel} and J_{\perp} are the photocurrent at the polarization angles of 0° and 90° with respect to the x direction. Given that the photoelectric response of pristine ML-HfGeTe₄ along the y direction depends on the sine function, i.e., J is almost 0 at 0°. According to the above ER equation, this result

will be infinite. Therefore, this kind of device along the y direction will not be considered here. As depicted in Fig. 7(a), the pristine ML-HfGeTe₄ exhibits a maximum ER of 98.94 at 2.9 eV, while the application of mechanical bending can increase it to 100.1 (indicated by the purple curve). However, this construction of heterostructure has a significant impact on the phase angle θ deviation and consequently reduces the maximum ER to 20.91, which is still much higher than the maximum ER (approximately 5) of the BP photodetector measured experimentally at present [77]. Moreover, the anisotropic ratio (AR), a crucial parameter of polarized optoelectronic devices, has been calculated systematically according to the definition of $[\max(J_x, J_y)/\min(J_x, J_y)]$, as illustrated in Fig. 7(b). The findings indicate that the pristine ML-HfGeTe₄ displays a maximum AR of 73 at 1.7 eV, which can be substantially enhanced by 22.98% by constructing heterostructure with anisotropic BP. This increase in the AR of the PGE photocurrent is attributed to the synergistic effect of strong in-plane anisotropy and ultralow symmetry. In contrast, mechanical bending marginally affects the AR of the pristine ML-HfGeTe₄ photodetector, reducing it by only 3.54%, demonstrating the robustness of the predicted anisotropic photoelectric devices against external forces.

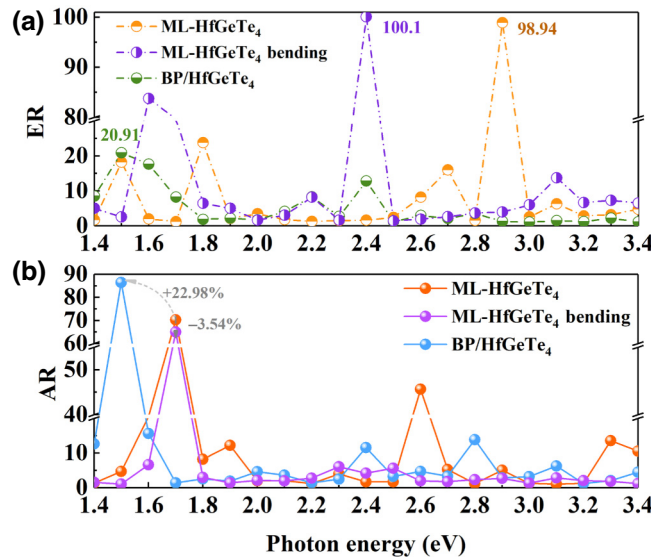


FIG. 7. (a) The extinction ratios (ER) and (b) anisotropic ratio (AR) of photocurrent for pristine ML-HfGeTe₄, bend ML-HfGeTe₄, and BP/HfGeTe₄.

To further elaborate on the remarkable functional coupling architecture and highlight the excellence of HfGeTe₄-based optoelectronic devices, we have compiled a summary of recent theoretical studies on the overall performance of the PGE photodetector in Table S1 within the Supplemental Material [58]. As is evident from the table, the amplitude of the PGE photocurrent in pristine HfGeTe₄ is several times greater than those of other pristine structures (indicated by the blue label). The reason behind this phenomenon is attributed to the quasi-one-dimensional fold structure of HfGeTe₄, which possesses only one symmetric operation for specular reflection and thus yields ultralow symmetry of C_s point group, a feature that is not present in other pristine structures. This means that the anisotropic pristine HfGeTe₄ already has C_s symmetry, therefore, other structures require the use of strategy, such as vacancy, doping, and strain. Furthermore, the synergistic effect of symmetry and anisotropy has been observed to further enhance the photoelectric response by applying mechanical bending and constructing heterostructure, and the loss of the corresponding asymmetry operation resulting from the change of symmetry from C_s to C_1 . As a consequence, the maximum photocurrent achieved in this case is 42.77, which far exceeds the currently known optoelectronic devices. On the other hand, the photoelectric AR of 73 in the pristine HfGeTe₄ remarkably surpasses other photodetectors, which are very attractive in the field of polarized photodetection. Despite the maximum ER achieved in this study of 100.1 is slightly lower than that reported in some other studies.

D. 2D BP/HfGeTe₄ for high-performance solar cells

Based on the aforementioned analysis, HfGeTe₄-based multifunctional devices exhibit significant potential as self-powered flexible optoelectronics and photodetectors with high photoresponsivity. In addition, we anticipate that the devices would demonstrate exceptional performance as solar cells in the field of solar-energy harvesting. Identifying a suitable material possessing high optical absorbance, high solar conversion efficiency, and low electron-hole recombination rate remains an essential challenge in the industrial implementation of 2D solar-energy-harvesting applications. Thus, the frequency-dependent dielectric functions (ϵ_2) and optical absorption coefficient of ML-HfGeTe₄ are calculated first, as shown in Fig. S8 within the Supplemental Material [58]. It is clear that the significant optical anisotropy can be directly observed, and the absorption spectrum of ML-HfGeTe₄ overlaps massively under the incident AM1.5 solar flux. The broad optical absorption range with high absorption coefficient ($4 \times 10^5 \text{ cm}^{-1}$) is close to the perovskites that are known to be highly efficient for solar cells [78].

Next, we examine the stability and electronic characteristics of BP/HfGeTe₄ heterostructure. The phonon dispersions have confirmed the dynamical stability of the constituent layers. To predict the thermal stability, AIMD simulations are conducted as illustrated in Fig. 8(a). The results show that no bond breaking or structural reconstruction occurred, and the total energy remained stable without showing any significant fluctuations, implying that BP/HfGeTe₄ are thermally stable. The projected band structures and density of states of BP/HfGeTe₄ are theoretically calculated using PBE methods, as shown in Fig. 8(b). It is found that BP/HfGeTe₄ has a direct band gap of 0.62 eV and a staggered type-II band alignment. The conduction-band minimum (CBM) and the valence-band maximum (VBM) are contributed separately by the BP and HfGeTe₄ monolayers, which is conducive to the effective separation of the photoexcited electron-hole pairs. The band decomposed charge densities of heterostructure demonstrates the contribution of isolated monolayers (see the resultant snapshot).

The charge redistribution at the interface can alter the electronic properties of type-II BP/HfGeTe₄ heterostructure. Figure 8(c) presents the corresponding planar averaged electrostatic potential with respect to the vacuum layer z with dipole correction. According to the band structures, the CBM of ML-HfGeTe₄ is higher than that of ML-BP, indicating that the charge-transfer process occurs from HfGeTe₄ (donor) to BP (acceptor). Consequently, a potential drop ($\Delta V = 8.85 \text{ eV}$) is established at the interfaces, giving rise to an effective built-in electric field (E_{int}) with HfGeTe₄ towards BP. The E_{int} significantly impacts the photoexcited carrier migration by efficiently separating the electron-hole pairs and restraining their

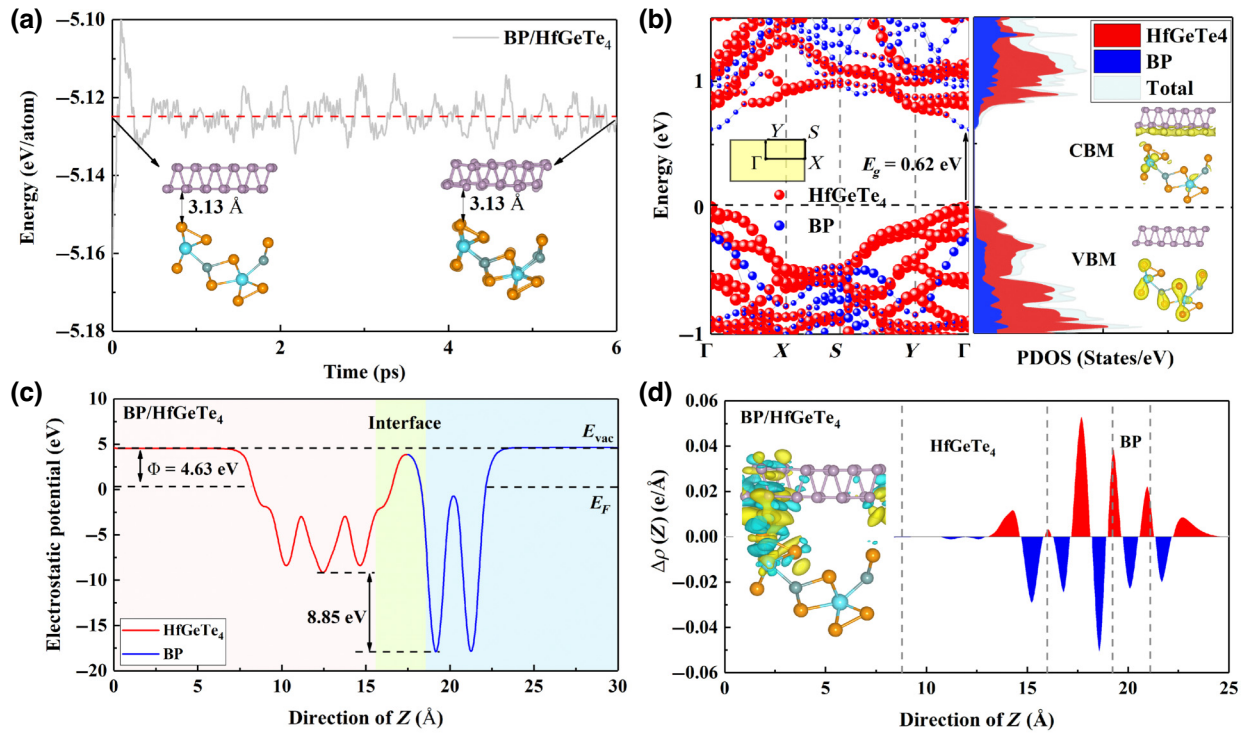


FIG. 8. (a) Variation of energy versus time at 300 K for BP/HfGeTe₄, the insets show the snapshots of atomic configurations at the start and end of AIMD simulations, (b) projected band structures and density of states of BP/HfGeTe₄. The illustration on the right shows the band decomposed charge densities of heterostructure, (c) planar-averaged electrostatic potential and (d) charge-density difference as a function of position in BP/HfGeTe₄ along the z direction. The 3D charge-density difference of BP/HfGeTe₄ with the isovalue of $1.0 \times 10^{-3} e \text{ \AA}^{-3}$, and the yellow and cyan denote the accumulation and depletion regions of electrons.

recombination. To gain more details of charge transfer and interface coupling in BP/HfGeTe₄, the charge-density difference, defined as $\Delta\rho = \rho_{\text{het}} - \rho_{\text{HfGeTe}_4} - \rho_{\text{BP}}$ with ρ_{het} , ρ_{HfGeTe_4} , and ρ_{BP} being charge densities of the heterostructure, isolated HfGeTe₄, and BP monolayers, respectively, is presented in Fig. 8(d). The oscillations show the charge-transfer status in space. It can be seen that the charge transfer occurs mainly at the heterointerface, and the regions of hole and electron accumulation are close to HfGeTe₄ and BP layers, respectively. The left illustration gives the three-dimensional (3D) differential charge density of BP/HfGeTe₄ with an isovalue of $1.0 \times 10^{-3} e \text{ \AA}^{-3}$, where yellow and cyan regions denote the accumulation and depletion of electrons. Note that the charge transfer is mainly distributed by the adjacent atomic layers owing to the interface dipole. Moreover, quantitative analysis technique based on Bader charges confirms that approximately 0.18 e are transferred from HfGeTe₄ to BP per unit cell.

Optical conductivity $\sigma_1(\omega)$ is an essential parameter for the development of photoelectric devices, especially in the fabrication of high-performance photosensitive photodetectors and efficient solar cells, which can be defined as $\sigma_1(\omega) = \omega\varepsilon_2(\omega)/4\pi$ with ω and ε_2 being the photon frequency and imaginary part of the dielectric function, respectively. Figure 9 illustrates the optical conductivity

of each layer and their type-II heterostructure. All three structures exhibit distinctive optical in-plane anisotropy characteristics in the x and y directions because of their intrinsic linear dichroism, with the optical conductivity primarily governed by the x direction within the visible light range. This finding is consistent with that

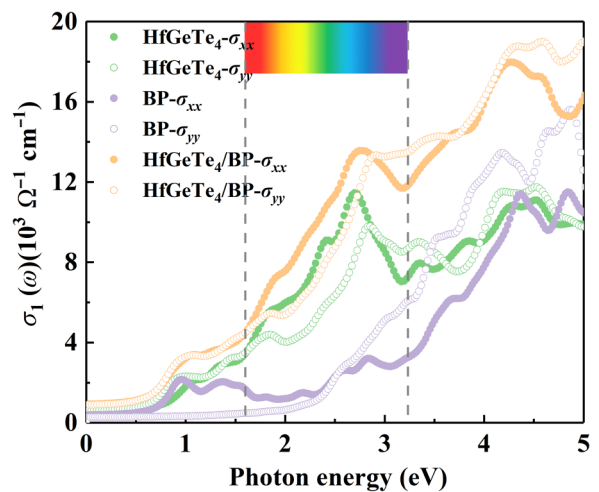


FIG. 9. Direction-dependent optical conductivity of ML-HfGeTe₄, ML-BP, and BP/HfGeTe₄.

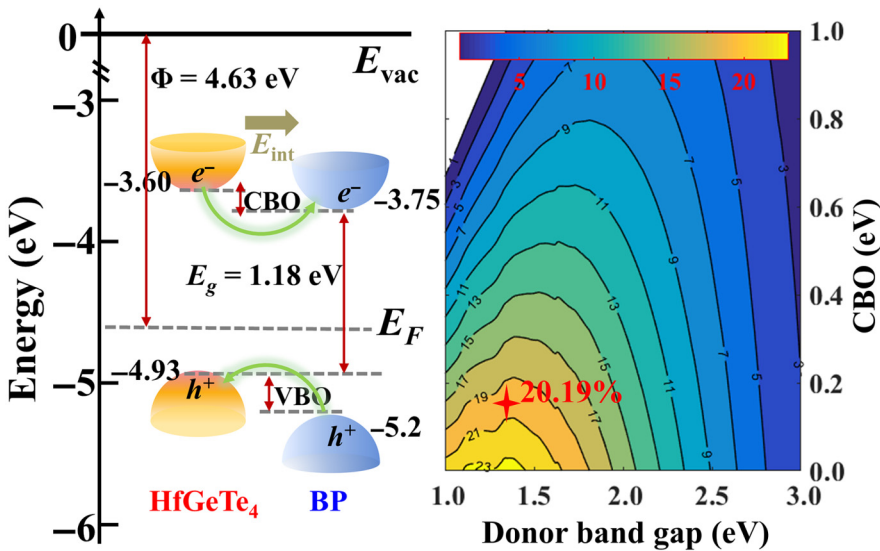


FIG. 10. (a) Photoexcited carrier migration and related parameters in a staggered type-II band alignment. (b) PCE contour as a function of donor band gap and CBO in the Anderson limit.

of PGE photocurrent. Besides, the optical conductivity of ML-HfGeTe₄ is significantly higher than that of ML-BP within the visible light range, suggesting that HfGeTe₄-based structures hold promise as a replacement for BP in anisotropic photoelectric devices. Compared with isolated monolayers, the optical conductivity of type-II heterostructure is enhanced from ultraviolet to near-infrared ranges. Notably, BP/HfGeTe₄ exhibits a peak optical conductivity of approximately $13 \times 10^3 \Omega^{-1} \text{ cm}^{-1}$ in the x direction within the visible light range, indicating its immense potential in solar-energy harvesting.

The evaluation of the PCE is a critical aspect in assessing the ability of a solar cell to convert solar energy. In 2006, Scharber *et al.* [79] proposed a method to calculate PCE in organic solar cells, which was subsequently adapted for use in 2D solar cells [80]. The theoretical maximum PCE can be estimated using the equation provided below:

$$\eta = \frac{J_{\text{sc}} V_{\text{oc}} \beta_{\text{FF}}}{P_{\text{solar}}} = \frac{0.65(E_g^d - \Delta E_c - 0.3) \int_{E_g^d}^{\infty} (J_{\text{ph}}(\hbar\omega)/\hbar\omega) d(\hbar\omega)}{\int_0^{\infty} J_{\text{ph}}(\hbar\omega) d(\hbar\omega)}, \quad (7)$$

where the band fill factor β_{FF} derived from the Shockley-Queisser limitation is 0.65, E_g^d is the donor band gap, and ΔE_c is the conduction-band offset (CBO) at the Anderson limit. $(E_g^d - \Delta E_c - 0.3)$ refers to the open-circuit voltage, where 0.3 is the empirical parameter of experimental fitting. $J_{\text{ph}}(\hbar\omega)$ (W/m²/eV) is the AM 1.5 M solar-energy flux at the photon energy ($\hbar\omega$). Given that the PCE exhibits a strong correlation with the donor band gap and CBO, the electronic band structures for BP/HfGeTe₄ are further refined using the HSE06 method to enhance their accuracy, as illustrated in Fig. S9(a) within the Supplemental

Material [58]. It shows that the overall band structures remain unaltered, but the band gap is increased to 1.18 eV.

To provide greater insight into the carrier migration at the interface and the driving forces behind the PCE, Fig. 10(a) presents the migration schematic of photoexcited electron-hole pairs in BP/HfGeTe₄. The work function of BP/HfGeTe₄, $\Phi = E_{\text{vac}} - E_F$, is 4.63 eV, where E_{vac} and E_F are the vacuum level and Fermi level, respectively. Meanwhile, the CBO and donor band gap are 0.15 and 0.23 eV. Interestingly, the PCE of BP/HfGeTe₄ can be up to 20.19%, as shown in Fig. 10(b), which is higher than those of other theoretical reports of heterobilayer solar cells, such as GeSe/SnS (approximately 18%) [81], Ga/In-based (10–13%) [82], Janus TMD/TMD (0.8–19.91%) [83], Ga₂SeTe/InS (17.7%) [9], and so forth.

Strain engineering is also regarded as a viable approach to regulate the electronic and optical characteristics, particularly the band alignment and PCE of heterostructure. Considering its experimental feasibility, we apply a 4% in-plane biaxial tensile strain to investigate its impact on the electronic properties of BP/HfGeTe₄ based on the HSE06 functional. The corresponding band structures are depicted in Fig. S9(b) within the Supplemental Material [58], in which the effective tunability of the band alignment and band gap by strain engineering is clearly demonstrated, that is, the band gap is reduced to 1.03 eV and the band alignment shifts from type II to type I. These outcomes augur well for BP/HfGeTe₄, which demonstrates multifunctional photoelectric properties and may be considered highly desirable candidate units for use in efficient solar cells and luminescent devices.

IV. CONCLUSIONS

To summarize, we propose a kind of multifunctional optoelectronic device that can integrate multiple gain effects. Under illumination with linearly polarized light,

a remarkably anisotropic PGE photocurrent can be generated in the pristine ML-HfGeTe₄ photodetector, rendering it self-powered. The photoelectric response can be further improved by an order of magnitude through mechanical bending due to the symmetry reduction from C_s to C_1 . Moreover, the AR and PGE photocurrent can be highly increased in BP/HfGeTe₄ heterostructure due to the synergistic effect of ultralow symmetry and anisotropy. Compared with isolated monolayers, the anisotropic optical conductivity of BP/HfGeTe₄ is improved from ultraviolet to near-infrared ranges. Our results present a fascinating functional coupling architecture that simultaneously realizes photodetection with high photoresponsivity and efficient solar-energy harvesting in 2D HfGeTe₄-based optoelectronic devices, bringing us closer to achieving the next-generation chip-scale integrated optoelectronics.

ACKNOWLEDGMENT

This work was supported by the National Natural Science Foundation of China (Grants No. U2001215 and No. 12174099). We gratefully acknowledge HZWTECH for providing computation facilities.

- [1] M. Buscema, D. J. Groenendijk, G. A. Steele, H. S. van der Zant, and A. Castellanos-Gomez, Photovoltaic effect in few-layer black phosphorus PN junctions defined by local electrostatic gating, *Nat. Commun.* **5**, 4651 (2014).
- [2] Y. Li, J. Fu, X. Mao, C. Chen, H. Liu, M. Gong, and H. Zeng, Enhanced bulk photovoltaic effect in two-dimensional ferroelectric CuInP₂S₆, *Nat. Commun.* **12**, 5896 (2021).
- [3] B. Feng, X. Pan, T. Liu, S. Tian, T. Wang, and Y. Chen, A broadband photoelectronic detector in a silicon nanopillar array with high detectivity enhanced by a monolayer graphene, *Nano Lett.* **21**, 5655 (2021).
- [4] L. Li, P. Yuan, T. Liu, Z. Ma, C. Xia, and X. Li, Self-powered broad band photodetector based on a monolayer InSe p-i-n homojunction, *Phys. Rev. Appl.* **19**, 014039 (2023).
- [5] M. O. Sauer, A. Taghizadeh, U. Petralanda, M. Ovesen, K. S. Thygesen, T. Olsen, H. Cornean, and T. G. Pedersen, Shift current photovoltaic efficiency of 2D materials, *npj Comput. Mater.* **9**, 35 (2023).
- [6] Z. Wang, P. Luo, B. Han, X. Zhang, S. Zhao, S. Wang, X. Chen, L. Wei, S. Yang, X. Zhou, S. Wang, X. Tao, and T. Zhai, Strong in-plane anisotropic SiP₂ as a IV–V 2D semiconductor for polarized photodetection, *ACS Nano* **15**, 20442 (2021).
- [7] S. Wu, Y. Chen, X. Wang, H. Jiao, Q. Zhao, X. Huang, X. Tai, Y. Zhou, H. Chen, X. Wang, S. Huang, H. Yan, T. Lin, H. Shen, W. Hu, X. Meng, J. Chu, and J. Wang, Ultrasensitive polarization-resolved black phosphorus homojunction photodetector defined by ferroelectric domains, *Nat. Commun.* **13**, 3198 (2022).
- [8] H. Jiang, J. Wei, F. Sun, C. Nie, J. Fu, H. Shi, J. Sun, X. Wei, and C. W. Qiu, Enhanced photogating effect in graphene photodetectors via potential fluctuation engineering, *ACS Nano* **16**, 4458 (2022).
- [9] K. Liang, T. Huang, K. Yang, Y. Si, H. Y. Wu, J. C. Lian, W. Q. Huang, W. Y. Hu, and G. F. Huang, Dipole engineering of two-dimensional van der Waals heterostructures for enhanced power-conversion efficiency: the case of Janus Ga₂SeTe/InS, *Phys. Rev. Appl.* **16**, 054043 (2021).
- [10] F. Zhang, *et al.*, Metastable Dion-Jacobson 2D structure enables efficient and stable perovskite solar cells, *Science* **375**, 71 (2022).
- [11] S. Zamani and R. Farghadan, Graphene nanoribbon spin-photodetector, *Phys. Rev. Appl.* **10**, 034059 (2018).
- [12] J. Kim, K. W. Kim, D. Shin, S. H. Lee, J. Sinova, N. Park, and H. Jin, Prediction of ferroelectricity-driven Berry curvature enabling charge- and spin-controllable photocurrent in tin telluride monolayers, *Nat. Commun.* **10**, 3965 (2019).
- [13] H. L. Wang, C. C. Cheng, L. Zhang, H. T. Liu, Y. Zhao, Y. L. Guo, W. P. Hu, G. Yu, and Y. Q. Liu, Inkjet printing short-channel polymer transistors with high-performance and ultrahigh photoresponsivity, *Adv. Mater.* **26**, 4683 (2014).
- [14] M. M. Furchi, D. K. Polyushkin, A. Pospischil, and T. Mueller, Mechanisms of photoconductivity in atomically thin MoS₂, *Nano Lett.* **14**, 6165 (2014).
- [15] C. Qian, J. Sun, L. A. Kong, G. Gou, M. Zhu, Y. Yuan, H. Huang, Y. Gao, and J. Yang, High-performance organic heterojunction phototransistors based on highly ordered copper phthalocyanine/para-sexiphenyl thin films, *Adv. Funct. Mater.* **27**, 1604933 (2017).
- [16] M. Cao, C. Zhang, Z. Cai, C. C. Xiao, X. S. Chen, K. Y. Yi, Y. G. Yang, Y. H. Lu, and D. C. Wei, Enhanced photoelectrical response of thermodynamically epitaxial organic crystals at the two-dimensional limit, *Nat. Commun.* **10**, 756 (2019).
- [17] H. Ma and M. Xue, Recent advances in the photothermal applications of two-dimensional nanomaterials: Photothermal therapy and beyond, *J. Mater. Chem. A* **9**, 17569 (2021).
- [18] W. Shockley, The theory of p-n junctions in semiconductors and p-n junction transistors, *ATT Tech. J.* **28**, 435 (1949).
- [19] Q. Guo, A. Pospischil, M. Bhuiyan, H. Jiang, H. Tian, D. Farmer, B. Deng, C. Li, S. J. Han, H. Wang, Q. Xia, T. P. Ma, T. Mueller, and F. Xia, Black phosphorus mid-infrared photodetectors with high gain, *Nano Lett.* **16**, 4648 (2016).
- [20] V. I. Belinicher and B. I. Sturman, The photogalvanic effect in media lacking a center of symmetry, *Sov. Phys. Usp.* **23**, 199 (1980).
- [21] S. Wang, H. Zhang, J. Zhang, S. Li, D. Luo, J. Wang, K. Jin, and J. Sun, Circular photogalvanic effect in oxide two-dimensional electron gases, *Phys. Rev. Lett.* **128**, 187401 (2022).
- [22] L. E. Golub and M. M. Glazov, Raman photogalvanic effect: Photocurrent at in elastic light scattering, *Phys. Rev. B* **106**, 205205 (2022).
- [23] Z. Zheng, L. Zhu, Z. Cao, X. Guo, Y. Wang, and K. Yao, The pure spin current and fully spin-polarized current induced by the photogalvanic effect and spin-Seebeck effect

- in halogen-decorated phosphorene, *Phys. Chem. Chem. Phys.* **25**, 3979 (2023).
- [24] R. von Baltz and W. Kraut, Theory of the bulk photovoltaic effect in pure crystals, *Phys. Rev. B* **23**, 5590 (1981).
- [25] T. Rangel, B. M. Fregoso, B. S. Mendoza, T. Morimoto, J. E. Moore, and J. B. Neaton, Large bulk photovoltaic effect and spontaneous polarization of single-layer monochalcogenides, *Phys. Rev. Lett.* **119**, 067402 (2017).
- [26] S. Rajpurohit, C. D. Pemmaraju, T. Ogitsu, and L. Z. Tan, Nonperturbative study of bulk photovoltaic effect enhanced by an optically induced phase transition, *Phys. Rev. B* **105**, 094307 (2022).
- [27] B. Kim, N. Park, and J. Kim, Giant bulk photovoltaic effect driven by the wall-to-wall charge shift in WS₂ nanotubes, *Nat. Commun.* **13**, 3237 (2022).
- [28] A. M. Glass, D. V. D. Linde, and T. J. Negran, High-voltage bulk photovoltaic effect and the photorefractive process in LiNbO₃, *Appl. Phys. Lett.* **25**, 233 (1974).
- [29] M. Nakamura, S. Horiuchi, F. Kagawa, N. Ogawa, T. Kurumaji, Y. Tokura, and M. Kawasaki, Shift current photovoltaic effect in a ferroelectric charge-transfer complex, *Nat. Commun.* **8**, 281 (2017).
- [30] J. E. Spanier, V. M. Fridkin, A. M. Rappe, A. R. Akbashev, A. Polemi, Y. Qi, Z. Gu, S. M. Young, C. J. Hawley, D. Imbrenda, G. Xiao, A. L. Bennett-Jackson, and C. L. Johnson, Power conversion efficiency exceeding the Shockley-Queisser limit in a ferroelectric insulator, *Nat. Photonics* **10**, 611 (2016).
- [31] M. M. Yang, D. J. Kim, and M. Alexe, Flexo-photovoltaic effect, *Science* **360**, 904 (2018).
- [32] Y. J. Zhang, T. Ideue, M. Onga, F. Qin, R. Suzuki, A. Zak, R. Tenne, J. H. Smet, and Y. Iwasa, Enhanced intrinsic photovoltaic effect in tungsten disulfide nanotubes, *Nature* **570**, 349 (2019).
- [33] C. M. Ji, D. Dey, Y. Peng, X. T. Liu, L. N. Li, and J. H. Luo, Ferroelectricity-driven self-powered ultraviolet photodetection with strong polarization sensitivity in a two-dimensional halide hybrid perovskite, *Angew. Chem., Int. Ed.* **59**, 18933 (2020).
- [34] Y. Peng, X. T. Liu, Z. H. Sun, C. M. Ji, L. N. Li, Z. Y. Wu, S. S. Wang, Y. P. Yao, M. C. Hong, and J. H. Luo, Exploiting the bulk photovoltaic effect in a 2D trilayered hybrid ferroelectric for highly sensitive polarized light detection, *Angew. Chem., Int. Ed.* **59**, 3933 (2020).
- [35] S. M. Young, F. Zheng, and A. M. Rappe, Prediction of a linear spin bulk photovoltaic effect in antiferromagnets, *Phys. Rev. Lett.* **110**, 057201 (2013).
- [36] Y. Q. Xie, M. Y. Chen, Z. W. Wu, Y. B. Hu, Y. Wang, J. Wang, and H. Guo, Two-dimensional photogalvanic spin-battery, *Phys. Rev. Appl.* **10**, 034005 (2018).
- [37] X. X. Tao, P. Jiang, H. Hao, X. H. Zheng, L. Zhang, and Z. Zeng, Pure spin current generation via photogalvanic effect with spatial inversion symmetry, *Phys. Rev. B* **102**, 081402(R) (2020).
- [38] L. Shu, L. Qian, X. Ye, and Y. Xie, Multifunctional two-dimensional VS₂N₄/WS₂N₄/VS₂N₄ photodetector driven by the photogalvanic effect, *Phys. Rev. Appl.* **17**, 054010 (2022).
- [39] Y. Li, X. Shang, Y. H. Zhou, and X. Zheng, Realizing pure spin current by the photogalvanic effect in armchair graphene nanoribbons with nano-constriction engineering, *Phys. Chem. Chem. Phys.* **25**, 2890 (2023).
- [40] J. Zhao, Y. B. Hu, Y. Q. Xie, L. Zhang, and Y. Wang, Largely enhanced photogalvanic effects in the phosphorene photodetector by strain-increased device asymmetry, *Phys. Rev. Appl.* **14**, 064003 (2020).
- [41] L. Y. Qian, J. Zhao, and Y. Q. Xie, Enhanced photogalvanic effect in the two-dimensional MgCl₂/ZnBr₂ vertical heterojunction by inhomogenous tensile stress, *Front. Phys.* **17**, 13502 (2022).
- [42] N. Sun, H. Ye, R. Quhe, Y. Liu, and M. Wang, Prediction of photogalvanic effect enhancement in Janus transition metal dichalcogenide monolayers induced by spontaneous curling, *Appl. Surf. Sci.* **619**, 156730 (2023).
- [43] Z. Xu, B. Luo, M. Chen, W. Xie, Y. Hu, and X. Xiao, Enhanced photogalvanic effects in the two-dimensional WTe₂ monolayer by vacancy- and substitution-doping, *Appl. Surf. Sci.* **548**, 148751 (2021).
- [44] X. Sun, S. Yin, D. Wei, Y. Li, Y. Ma, and X. Dai, Effect of vacancies on photogalvanic effect in two-dimensional WSe₂ photodetector, *Appl. Surf. Sci.* **610**, 155401 (2023).
- [45] M. Sun, J. Liu, and F. Chi, Photogalvanic effects in Janus monolayer In₂SSe with vacancy defects, *Phys. E* **145**, 115467 (2023).
- [46] Y. Xie, L. Zhang, Y. Zhu, L. Liu, and H. Guo, Photogalvanic effect in monolayer black phosphorus, *Nanotechnology* **26**, 455202 (2015).
- [47] P. P. Liu, Z. G. Shao, W. M. Luo, and M. Yang, Photogalvanic effect in chromium-doped monolayer MoS₂ from first principles, *Phys. E* **128**, 114577 (2020).
- [48] M. Nakamura, F. Kagawa, T. Tanigaki, H. S. Park, T. Matsuda, D. Shindo, Y. Tokura, and M. Kawasaki, Spontaneous polarization and bulk photovoltaic effect driven by polar discontinuity in LaFeO₃/SrTiO₃ heterojunctions, *Phys. Rev. Lett.* **116**, 156801 (2016).
- [49] S. S. Li, T. Wang, X. S. Chen, W. Lu, Y. Q. Xie, and Y. B. Hu, Self-powered photogalvanic phosphorene photodetectors with high polarization sensitivity and suppressed dark current, *Nanoscale* **10**, 7694 (2018).
- [50] T. Akamatsu, T. Ideue, L. Zhou, Y. Dong, S. Kitamura, M. Yoshii, D. Yang, M. Onga, Y. Nakagawa, K. Watanabe, T. Taniguchi, J. Laurienzo, J. Huang, Z. Ye, T. Morimoto, H. Yuan, and Y. Iwasa, A van der Waals interface that creates in-plane polarization and a spontaneous photovoltaic effect, *Science* **372**, 68 (2021).
- [51] Y. M. Zhang, R. G. Cao, Y. B. Hu, Y. Wang, and Y. Q. Xie, A promising polarization-sensitive ultraviolet photodetector based on the two-dimensional ZrNBr-ZrNCl lateral heterojunction with enhanced photoresponse: A theoretical prediction, *Appl. Surf. Sci.* **560**, 149907 (2021).
- [52] A. Mar and J. A. Ibers, The layered ternary germanium tellurides ZrGeTe₄, HfGeTe₄, and TiGeTe₆: structure, bonding, and physical properties, *J. Am. Chem. Soc.* **115**, 3227 (1993).
- [53] Y. Saito and J. Robertson, Direct transition of a HfGeTe₄ ternary transition-metal chalcogenide monolayer with a zigzag van der Waals gap, *APL Mater.* **6**, 046104 (2018).
- [54] M. L. Adam, O. A. Moses, Z. U. Rehman, Z. Liu, L. Song, and X. Wu, Band gap engineering of monolayer ZrGeTe₄

- via strain: A first-principles study, *Mater. Chem. Phys.* **253**, 123308 (2020).
- [55] P. Guo, J. Liang, B. Zhou, W. Wang, and Z. Liu, Strong anisotropy and layer-dependent carrier mobility of two-dimensional semiconductor $ZrGeTe_4$, *J. Phys.: Condens. Matter* **32**, 325502 (2020).
- [56] H. R. Banjade, J. Pan, and Q. Yan, Monolayer 2D semiconducting tellurides for high-mobility electronics, *Phys. Rev. Mater.* **5**, 014005 (2021).
- [57] D. Xu, J. Tan, H. Hu, and G. Ouyang, First-principles investigation of in-plane anisotropies in XYTe₄ monolayers with X = Hf, Zr, Ti and Y = Si, Ge, *Phys. Chem. Chem. Phys.* **24**, 22806 (2022).
- [58] See Supplemental Material at <http://link.aps.org/supplemental/10.1103/PhysRevApplied.20.054025> for computational details (schematic diagram of device, phonon band dispersions, electronic band structures, photocurrent of different supercells, k -point grids and bending strain, optical absorption coefficient, conversion of normalized currents). Additional calculations concerning the comparison between our job and previous work are also included, which includes Refs. [59,60].
- [59] P. Zhao, J. Li, W. Wei, Q. Sun, H. Jin, B. Huang, and Y. Dai, Giant anisotropic photogalvanic effect in a flexible AsSb monolayer with ultrahigh carrier mobility, *Phys. Chem. Chem. Phys.* **19**, 27233 (2017).
- [60] T. Wang, F. Chi, M. Chen, and J. Liu, Giant photogalvanic effect in Janus monolayer In₂SSe, *Opt. Commun.* **492**, 126945 (2021).
- [61] P. E. Blochl, Projector augmented-wave method, *Phys. Rev. B* **50**, 17953 (1994).
- [62] G. Kresse and J. Hafner, *Ab initio* molecular dynamics for liquid metals, *Phys. Rev. B* **47**, 558 (1993).
- [63] J. P. Perdew, K. Burke, and M. Ernzerhof, Generalized gradient approximation made simple, *Phys. Rev. Lett.* **77**, 3865 (1996).
- [64] H. J. Monkhorst and J. D. Pack, Special points for Brillouin-zone integrations, *Phys. Rev. B* **13**, 5188 (1976).
- [65] A. Togo and I. Tanaka, First principles phonon calculations in materials science, *Scr. Mater.* **108**, 1 (2015).
- [66] V. Wang, N. Xu, J. C. Liu, G. Tang, and W. T. Geng, VASP-KIT: A user-friendly interface facilitating high-throughput computing and analysis using VASP code, *Comput. Phys. Commun.* **267**, 108033 (2021).
- [67] J. Taylor, H. Guo, and J. Wang, *Ab initio* modeling of quantum transport properties of molecular electronic devices, *Phys. Rev. B* **63**, 245407 (2001).
- [68] L. E. Henrickson, Nonequilibrium photocurrent modeling in resonant tunneling photodetectors, *J. Appl. Phys.* **91**, 6273 (2002).
- [69] J. Chen, Y. Hu, and H. Guo, First-principles analysis of photocurrent in graphene PN junctions, *Phys. Rev. B* **85**, 155441 (2012).
- [70] S. D. Ganichev, H. Ketterl, W. Prettl, E. L. Ivchenko, and L. E. Vorobjev, Circular photogalvanic effect induced by monopolar spin orientation in p-GaAs/AlGaAs multiple-quantum wells, *Appl. Phys. Lett.* **77**, 3146 (2000).
- [71] F. Xia, H. Wang, and Y. Jia, Rediscovering black phosphorus as an anisotropic layered material for optoelectronics and electronics, *Nat. Commun.* **5**, 4458 (2014).
- [72] Z. Luo, J. Maassen, Y. Deng, Y. Du, R. P. Garrels, M. S. Lundstrom, P. D. Ye, and X. Xu, Anisotropic in-plane thermal conductivity observed in few-layer black phosphorus, *Nat. Commun.* **6**, 8572 (2015).
- [73] R. Fei and L. Yang, Strain-engineering the anisotropic electrical conductance of few-layer black phosphorus, *Nano Lett.* **14**, 2884 (2014).
- [74] H. Yuan, X. Liu, F. Afshinmanesh, W. Li, G. Xu, J. Sun, B. Lian, A. G. Curto, G. Ye, Y. Hikita, Z. Shen, S. C. Zhang, X. Chen, M. Brongersma, H. Y. Hwang, and Y. Cui, Polarization-sensitive broadband photodetector using a black phosphorus vertical p-n junction, *Nat. Nanotechnol.* **10**, 707 (2015).
- [75] J. Wu, G. K. W. Koon, D. Xiang, C. Han, C. T. Toh, E. S. Kulkarni, I. Verzhbitskiy, A. Carvalho, A. S. Rodin, S. P. Koenig, G. Eda, W. Chen, A. H. C. Neto, and B. Ozilmez, Colossal ultraviolet photoresponsivity of few-layer black phosphorus, *ACS Nano* **9**, 8070 (2015).
- [76] Y. Li, S. Yang, and J. Li, Modulation of the electronic properties of ultrathin black phosphorus by strain and electrical field, *J. Phys. Chem. C* **118**, 23970 (2014).
- [77] N. Youngblood and M. Li, Ultrafast photocurrent measurements of a black phosphorus photodetector, *Appl. Phys. Lett.* **110**, 051102 (2017).
- [78] M. Shirayama, H. Kadokawa, T. Miyadera, T. Sugita, M. Tamakoshi, M. Kato, T. Fujiseki, D. Murata, S. Hara, T. N. Murakami, S. Fujimoto, M. Chikamatsu, and H. Fujiwara, Optical transitions in hybrid perovskite solar cells: Ellipsometry, density functional theory, and quantum efficiency analyses for $CH_3NH_3PbI_3$, *Phys. Rev. Appl.* **5**, 014012 (2016).
- [79] M. C. Scharber, D. Mühlbacher, M. Koppe, P. Denk, C. Waldauf, A. J. Heeger, and C. J. Brabec, Design rules for donors in bulk-heterojunction solar cells-towards 10% energy-conversion efficiency, *Adv. Mater.* **18**, 789 (2006).
- [80] C. C. Tho, C. Yu, Q. Tang, Q. Wang, T. Su, Z. Feng, Q. Wu, C. V. Nguyen, W. L. Ong, S. J. Liang, S. D. Guo, L. Cao, S. Zhang, S. A. Yang, L. K. Ang, G. Wang, and Y. S. Ang, Cataloguing MoSi₂N₄ and WSi₂N₄ van der Waals heterostructures: An exceptional material platform for excitonic solar cell applications, *Adv. Mater. Inter.* **10**, 2201856 (2022).
- [81] X. Lv, W. Wei, C. Mu, B. Huang, and Y. Dai, Two-dimensional GeSe for high performance thin-film solar cells, *J. Mater. Chem. A* **6**, 5032 (2018).
- [82] A. Rawat, R. Ahammed, Dimple, N. Jena, M. K. Mohanta, and A. De Sarkar, Solar energy harvesting in type II van der Waals heterostructures of semiconducting group III monochalcogenide monolayers, *J. Phys. Chem. C* **123**, 12666 (2019).
- [83] A. Rawat, M. K. Mohanta, N. Jena, Dimple, R. Ahammed, and A. De Sarkar, Nanoscale interfaces of Janus monolayers of transition metal dichalcogenides for 2D photovoltaic and piezoelectric applications, *J. Phys. Chem. C* **124**, 10385 (2020).